

# Computational and Experimental Investigation of Camber Morphing Airfoils for Reverse Flow Drag Reduction on High-Speed Rotorcraft

**George Jacobellis\***

PhD candidate

Center for Mobility with Vertical Lift (MOVE)

Rensselaer Polytechnic Institute

**Farhan Gandhi**

Professor

**Thomas Rice**

PhD candidate

Center for Flow Physics and Control

Rensselaer Polytechnic Institute

**Michael Amitay**

Professor

## ABSTRACT

Through computational fluid dynamics simulations and wind tunnel tests this study examines a NACA63-218 airfoil in reverse flow at  $Re = 375,000$ , and demonstrates reduction in reverse flow drag through the introduction of reflex camber when the airfoil is pitched nose up in reverse flow. Of the three dominant sources of reverse flow drag - ram pressure on the upper surface near the trailing-edge, suction on the lower surface near the trailing-edge, and bluff body separation at the rounded nose, reflex camber influences the first two, while leaving the third mostly unaffected. The change in trailing-edge geometry reduces exposure to ram drag on the upper surface while the suction on the lower surface rotates to result in a force opposite to the direction of the free stream. Although the 2D CFD simulations (URANS with SA turbulence model) had difficulty predicting the bluff body separation at the airfoil nose well, the change in flow at the trailing-edge was well captured yielding drag reductions of around 60% for a  $10^\circ$  reflex camber (compared to reductions of around 50% in the wind-tunnel test). Even greater percentage reductions in drag (up to 70%) were observed with a larger  $15^\circ$  reflex angle for nose-up pitch angles greater than  $5^\circ$  in reverse flow. With simulations at a higher Reynolds number (1.5 million) showing very similar drag reductions, using reflex camber over inboard blade sections appears to have significant promise for alleviating reverse flow drag on edgewise rotors at high advance ratio.

## INTRODUCTION

In recent years there has been tremendous interest in extending the maximum forward speed of rotary-wing aircraft operating with edgewise rotors to around 250 kts. Two configurations that have been heavily studied are the slowed rotor compound and the lift-offset coaxial configurations. In both cases, constraints on the maximum advancing tip Mach number require that the main rotor progressively slow down as the forward speed increases. The increasing forward speed combined with the reduction in rotor RPM results in rapid increases in advance ratio, and the high advance ratio (approaching 1, or greater) puts large inboard sections of the retreating blade in reverse flow, the phenomena whereby air flows from the sharp trailing-edge of the blade toward the rounded leading edge. To mitigate this adverse aerodynamic condition, slowed rotor compound helicopters transfer the majority of the lifting function to the wing in high-speed flight, while lift-offset coaxial helicopters transfer the lifting function to the advancing side of each of its counter-rotating rotors.

Despite significantly offloading the entire rotor (for the slowed rotor compound helicopters) or the retreating side (for lift-offset coaxial helicopters), the reverse flow region still remains hugely problematic; generating negative lift, large amounts of drag (which increases rotor H-force and reduces rotor  $L/D_e$ ), and high vibratory loads on the blades, pitch links and rotor hub. In the development of the X2TD, Sikorsky Aircraft Corporation introduced very specific design changes on the rotor blades targeted towards improvement in the reverse flow region (Ref. 1). Compared to the more conventional blades on the XH-59A, Sikorsky's previous coaxial helicopter from the 1970's, the X2TD blades had a lower chord in the inboard region, a lower pitch, and used double-ended airfoils. Figure 1 shows a schematic comparison of the operating states of these airfoils in reverse flow. While all of these changes were beneficial for the reverse flow region, they can be expected to be significantly detrimental to hover performance (recall that high pitch and chord is desirable over the inboard sections of the blade in hover). Additionally, using double-ended airfoils on the inboard blade sections to address reverse flow will result in even more lift being generated outboard in hover, yielding a further increase in rotor induced power. A recent study by Giovanetti and Hall (Ref. 2) suggests that a

\*corresponding author. Submitted for the AHS 74th Annual Forum, Phoenix, AZ, USA, May 15-17, 2018.

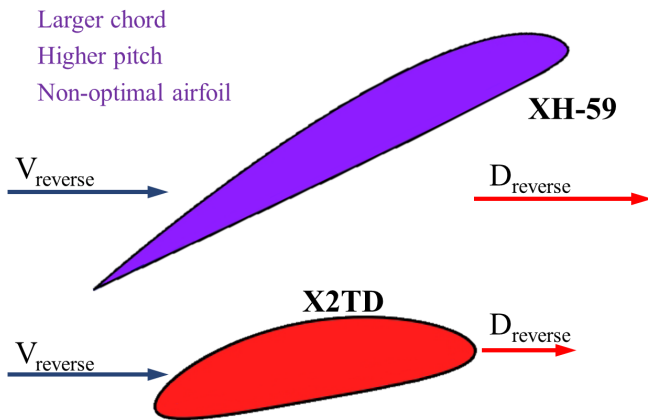


Fig. 1: Comparison of X2TD and XH-59A airfoils in reverse

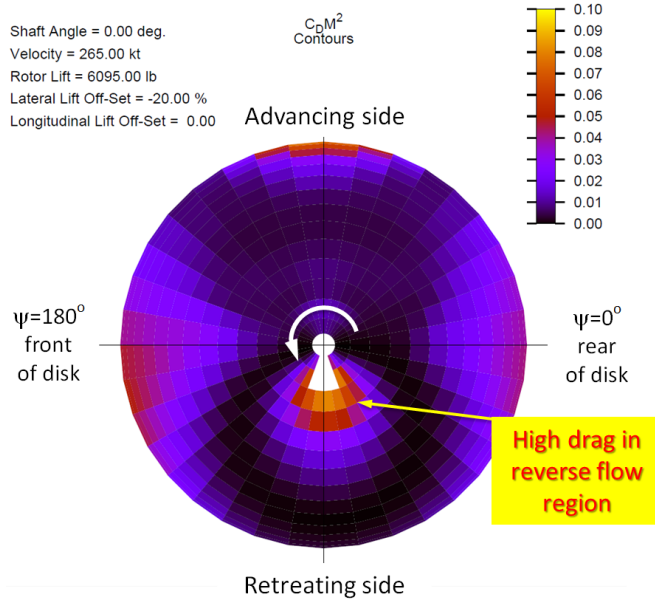


Fig. 2: Large region of reverse flow drag on retreating side of a high-speed coaxial rotor (Ref. 1)

coaxial rotor optimized for high speed can incur a 7% hover figure of merit penalty. Similarly, results from Hersy, Sridharan, and Celi (Ref. 3) show that an optimal design for high-speed increases hover power requirement by several 100s of HP on a 20,000 lb coaxial rotor helicopter.

At the airfoil level, a number of researchers have conducted fundamental studies to better understand behavior in the reverse flow regime. NACA conducted wind tunnel tests of reflex cambered airfoils (NACA 2212 and NACA M6) in reverse flow at  $Re = 0.4$  million (Ref. 4) as well as symmetric airfoils (NACA 0012) airfoils in reverse flow at  $Re = 0.5 - 1.8$  million (Ref. 5). Pope conducted experiments on a NACA 0015 at  $Re = 1.2$  million, including making surface pressure measurements (Ref. 6).

Leishman performed wind tunnel measurements on an SC1095 in reverse flow (Ref. 7) and showed that, compared to forward flow, the airfoil stalled earlier leading to higher drag as the angle of attack deviated from  $180^\circ$ . It was also reported that the drag near  $180^\circ$  was larger than the drag near  $0^\circ$  due to

the large amount of bluff body separation around the nose of the airfoil. Additionally, the pitching moments about the  $1/4$  chord were seen to be very large compared to forward flow as the center of lift moved closer to the  $3/4$  chord point when the airfoil was subjected to reverse flow.

Lind et. al. (Refs. 8, 9) made wind tunnel measurements including flow visualizations of a traditional NACA 0012 as well as two elliptical airfoils held at static angles of attack angles of attack through  $360^\circ$  at a Reynolds number of  $1.1 \times 10^5$ . They showed that the drag of a NACA 0012 airfoil in reverse flow is more than twice as large compared to forward flow due to early onset of flow separation, whereas the drag of an elliptical airfoil at moderate angles of attack ( $\alpha = 5^\circ - 15^\circ$ ) in reverse flow is significantly lower than the NACA 0012 in reverse flow.

In Ref. 10, Lind and Jones explored the vortex shedding characteristics of these airfoils at static angles of attack. They used time-resolved particle image velocimetry and smoke flow visualization to identify three reverse flow wake regimes: slender body vortex shedding at low angles of attack, turbulent wake at moderate angles of attack, and deep stall vortex shedding at larger angles of attack. Their work provided fundamental insight for rotor applications where flow separation and vortex shedding due to reverse flow can lead to unsteady loading, vibrations, and fatigue.

More recently, Lind et al. (Ref. 11) conducted an experimental investigation of Reynolds number effects in both forward and reverse flow. They showed that the loads for a NACA 0012 in reverse flow are relatively insensitive to Reynolds number due to early flow separation, whereas the loads of a thicker airfoil (NACA 0024) were found to be more sensitive to Reynolds number. Flow visualizations showing regions of attached and separated flow were shown, as well as laminar and turbulent regions on the elliptical airfoil. For the sharp trailing-edge airfoils in reverse flow, the flow separated at the sharp trailing-edge and then reattached further along the chord of the airfoil, before separating again near the nose of the airfoil. The unsteady characteristics of these airfoils through all static angles of attack were investigated by Lind and Jones in Ref. 12. They used surface pressure measurements and high speed particle image velocimetry to measure the unsteady behavior of the airloads and surrounding flowfield.

The effect of a dynamically pitching airfoil in reverse flow was also investigated by Smith et. al. (Ref. 13). They characterized the evolution of reverse flow dynamic stall and its sensitivity to pitch and flow parameters, where the type of dynamic stall observed (i.e., number of vortex structures) varied with change in reduced frequency and maximum pitch angle.

There have also been several numerical investigations on reverse flow to date. Smith et. al (Ref. 14) compared CFD solutions to several reverse flow airfoil experiments at high and reverse angles of attack including those of Pope, Critzos, and Leishman (Refs. 5-7). Both 2D RANS and Hybrid RANS/LES (HRLES) models were used, and the 2D RANS simulations were shown to have comparable accuracy to the HRLES solutions at low to moderate airfoil pitch angles in

reverse flow with substantially reduced computational time. Hodora and Smith extended the numerical study to various Mach numbers and yaw angles in Ref. 15.

A collaborative experimental and numerical investigation of airfoils in reverse flow conducted by Hodora et al. (Ref. 16) further characterized the performance of airfoils in reverse flow by comparing simulations with the experiments performed by Lind et. al. in Ref. 9. The authors successfully predicted the presence of the three unsteady wake regimes shown experimentally in Ref. 10. They showed that at angles of attack from about  $\alpha = 170^\circ - 190^\circ$  ( $\pm 10^\circ$  in reverse flow) both 2D RANS and HRLES simulations compared well with the experiments from Ref. 9, reinforcing the result from Ref 14 that 2D RANS is can provide good performance predictions at low to moderate reverse flow angles of attack. Ref. 16 also included an investigation of a two-dimensional NACA 0012 airfoil dynamically pitched through stall in reverse flow and compared with the experimental results in Ref. 13.

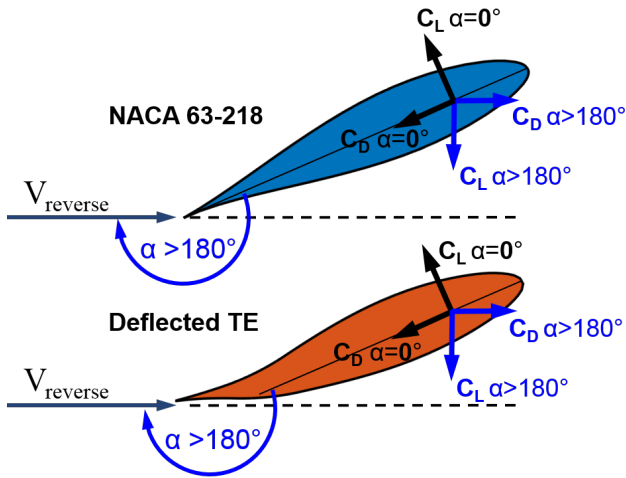


Fig. 3: Baseline NACA 63-218 and NACA 63-218 with reflex cambered trailing-edge. The orientation of the lift and drag vectors relative to the airfoil at zero angle of attack are shown in black and at  $\alpha > 180^\circ$  angle of attack are shown in blue.

While many of the previous studies (Refs. 7-16) focused on understanding airfoil behavior in reverse flow, there has been little effort directed toward mitigating the poor performance in this regime. Sikorsky’s solution of using elliptical airfoils inboard on the X2TD (along with reduced inboard blade pitch and chord) still yielded large drag in the reverse flow region (Figure 2) while being detrimental to hover performance. The present study seeks to investigate whether classical airfoils, with camber morphing capability, could be useful in mitigating reverse flow drag. Such classical airfoils on the inboard sections of the blade would result in substantially improved hover and low-speed performance compared to the double-ended airfoils on modern coaxial rotor designs. Using reflex camber in reverse flow conditions on an airfoil with a nose-up pitch attitude has the potential to reduce reverse flow drag substantially by more closely aligning the trailing-edge to the oncoming flow, as shown in Figure 3. In the present

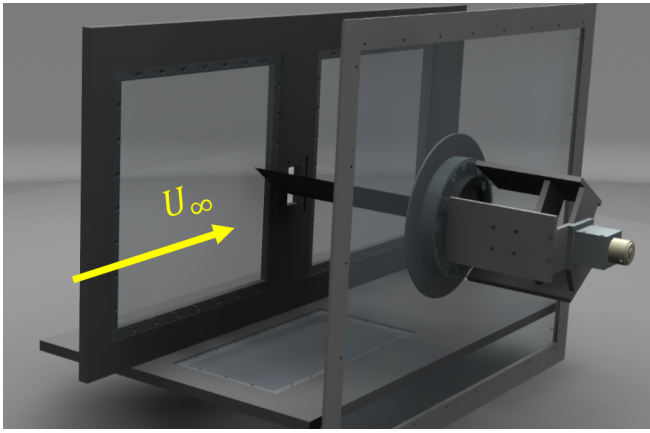
study, possible reductions in reverse flow drag are examined through a combination of wind-tunnel tests and CFD simulations. Specifically, the performance of a NACA 63-218 airfoil (which is one of the airfoils used on the XH-59A) in reverse flow is compared to that of a modified NACA 63-218 airfoil with reflex camber over a 25% chord section at the trailing-edge (shown in Figure 3).

## EXPERIMENTAL SETUP

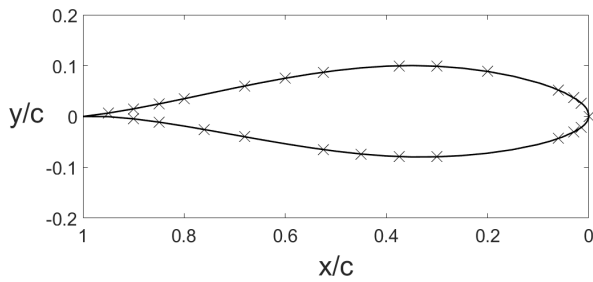
Wind tunnel experiments were conducted at the Center for Flow Physics and Control’s open return, subsonic wind tunnel at RPI. The wind tunnel was rated to have a maximum turbulence intensity less than 0.2% at its maximum speed of 50 m/s. Two airfoils models were fabricated, one of a baseline NACA 63-218 airfoil, and a second of a modified NACA 63-218 airfoil with a  $10^\circ$  upward reflex camber over a 25% chord section near the trailing-edge (shown in Figure 3). The models were fabricated with additive manufacturing, specifically utilizing stereo-lithography, with a resolution of 0.03 mm, and had chord  $c = 0.28$  m and span  $b = 0.46$  m. A schematic of the wind tunnel setup is shown in Figure 4a, where the flow is from bottom left to top right, and the model is shown to be placed at an arbitrary angle of attack. The model is rigidly connected to a DC motor, shown in the right hand side of Figure 4a, which allows for changes in angle of attack. A wall was placed 1mm from the tip to prevent the tip vortex from forming while still allowing the model to rotate.

The wind tunnel was operated at a speed of 20 m/s, corresponding to a Reynolds number  $Re_c = 375,000$  and  $Ma = 0.058$ . Tufts flow visualizations were obtained to show general trends associated with flow separation and reattachment. 7 rows of tufts were placed and the suction side of the airfoil, where each tuft was 2.5 cm in length, and were spaced 2cm apart from each other in the spanwise direction to visually determine locations of separation and unsteadiness. Surface pressure measurements were obtained using three Scanivalve model DSA3217 pressure scanners, and were sampled at 125 Hz for 10s. Figure 4 shows a wire-frame cross-section of the baseline airfoil to indicate the location of surface pressure ports. The surface pressure measurements were integrated to obtain the lift and drag forces on the airfoil due to pressure forces.

The pressure coefficient was linearly interpolated between the measurement points for the lift and drag integration. Due to the thin trailing-edge, the closest pressure measurement to the trailing-edge was at 95% chord on the upper surface and 90% chord on the lower surface. Pressure coefficient at the trailing-edge was extrapolated using the value at the closest measurement and an estimated value of the pressure at the trailing-edge based on the experimental data and CFD simulations. In most cases The flow will stagnate near the trailing-edge on either the upper surface or the lower surface, depending on the orientation of these surfaces relative to the flow, so the pressure at the trailing-edge on this surface was set to  $C_p = 1$ . The trailing-edge pressure coefficient on surfaces not experiencing flow stagnation were estimated based on the measurement



(a)



(b)

Fig. 4: Schematic of wind tunnel model, with flow from bottom left to top right (a), and location of pressure ports along NACA 63-218 airfoil (b).

nearest the trailing-edge and the CFD simulations.

## NUMERICAL SETUP AND METHODOLOGY

Transient simulations of the unsteady Navier-Stokes equations were run with the Kestrel Computational Fluid Dynamics Solver (KCFD) within the Helios framework (Ref. 17). KCFD is an unstructured, finite volume solver used extensively by the Air Force and other researchers. At a Reynolds number of 375,000, boundary layers for attached flow are expected to be laminar. However for an airfoil with a sharp trailing-edge in reverse flow, separation is expected over the sharp trailing-edge, as shown by Lind in Refs. 9 and 11. This separation can cause transition to turbulence at very low Reynolds numbers. Because the flow is expected to have regions of laminar and turbulent flow, as well as large separation regions, three methods of simulation are employed: two dimensional unsteady Navier-Stokes (N-S), two dimensional unsteady Reynolds Averaged Navier-Stokes (URANS) incorporating the Spalart-Allmaras (SA) turbulence model, and three dimensional Detached Eddy Simulation (DES) also incorporating the SA turbulence model.

Unstructured, tetrahedral grids were generated for the baseline as well as the reflex cambered geometries. The two

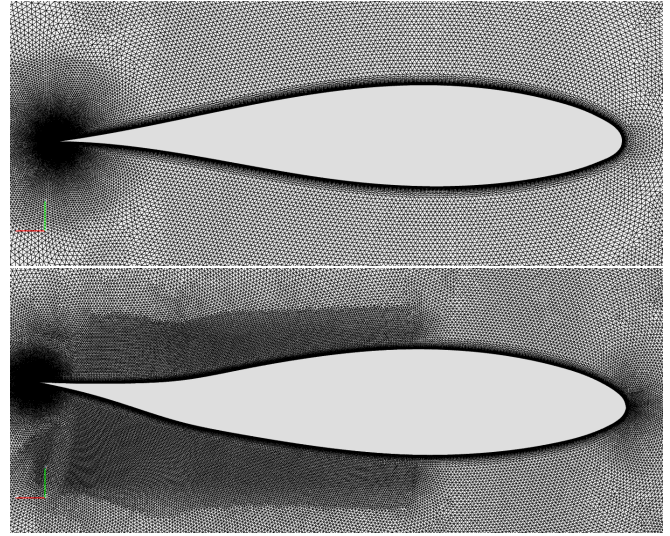


Fig. 5: CFD meshes for baseline NACA 63-218 (top) and variant with 10° reflex camber (bottom)

meshes are shown in Figure 5. The domain for the two dimensional simulations was made to be one cell thick in the span wise direction, With symmetry boundary conditions on either end. The domain for the three dimensional simulations was 60 cells thick resulting in 60 times the number of nodes as the 2D mesh, with a span of 0.25c. The computational domain extends 25 chords away from the airfoil in the normal direction, with a circular outer boundary. The meshes incorporated a 25 element thick boundary layer with a growth rate of 1.25 and a first element height of  $1.6 \times 10^{-5}$ m, corresponding to  $y^+ = 1$ . Additional refinement was made near the airfoil surface ensuring that the maximum element size was less than 0.7%c near the surface of the airfoil. The two dimensional mesh for the baseline airfoil has 782 nodes on the airfoil surface and 115,567 nodes resolving the computational domain. The reflexed airfoil has 783 nodes on the airfoil surface and 101,124 nodes resolving the domain. Simulations were run with a time step of .0001 sec, corresponding to 140 steps per chord traverse. Spatial and temporal discretization are second-order accurate.

## RESULTS

### Experimental study of NACA 63-218 with and without 10° Reflex Camber

The surface pressure was measured on both the Baseline NACA 63-218 model as well as the variant with a 10° upward deflection of the trailing at angles of attack from  $180^\circ < \alpha < 195^\circ$  (corresponding to  $0^\circ$  -  $15^\circ$  nose up in reverse flow) for the baseline airfoil and  $184^\circ < \alpha < 195^\circ$  for the reflex cambered airfoil. The wind tunnel was set at a speed of 20 m/s, corresponding to a Reynolds number  $Re_c = 375,000$  and Mach 0.058. Figure 6 shows the reverse flow lift, drag, and moment measured for the baseline and reflex cambered airfoil, computed by integrating the pressure measurements. With reflex camber, the lift coefficient is slightly reduced at angles

of attack below  $190^\circ$ , and is greater at angles of attack above  $190^\circ$ . Note that a positive lift coefficient will be acting downwards for an airfoil in reverse flow (refer to Figure 3). It is immediately evident that the experimental data show a drag reduction realized at angles of attack from  $184^\circ < \alpha < 195^\circ$ . Specifically, there is a pressure drag reduction up to 50% near  $\alpha = 190^\circ$  from  $C_D \sim 0.13$  to  $C_D \sim 0.06$ , due to the deflection of the trailing-edge section. This drag reduction will be further examined in the following discussion.

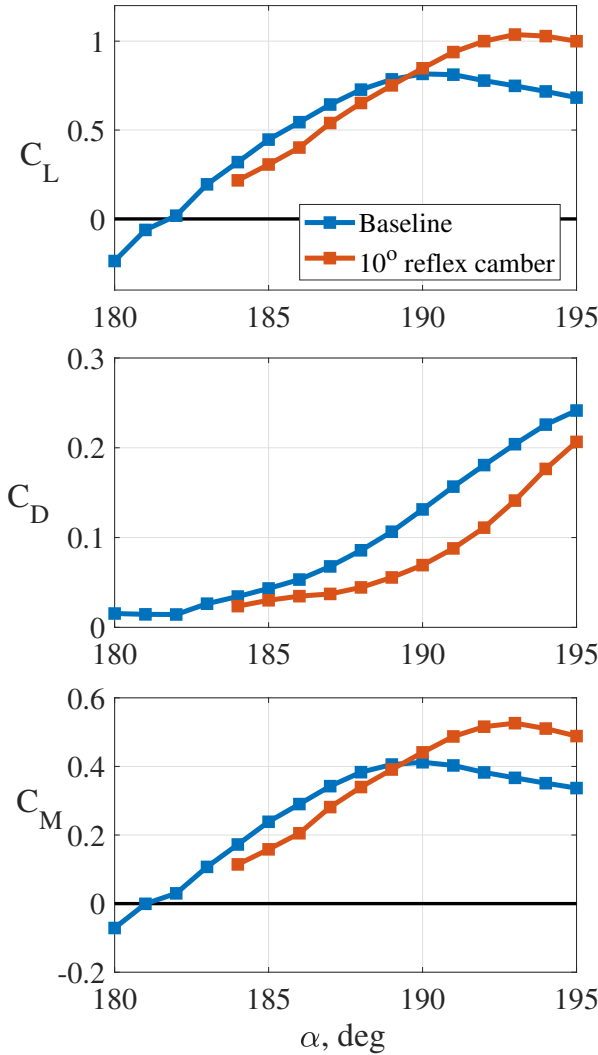


Fig. 6: Experimentally obtained pressure lift, drag, and moment coefficients about the airfoil quarter-chord on the NACA 63-218 with and without  $10^\circ$  deflection of the trailing-edge section (reflex camber)

The nose-up pitching moment about the airfoil quarter chord shows similar trends to the lift. An explanation for this is that the center of lift for an airfoil in reverse flow moves from the  $1/4$  chord to the  $3/4$  chord, as reported in Ref. 7.

Figure 7 shows the surface pressure coefficient measured during the experiment for the baseline and reflex cambered air-

foils at  $\alpha = 190^\circ$ . Each dot corresponds to a single time-averaged pressure measurement and the lines represent the interpolation used for integration. In this figure, the blue line represents the lower surface of the airfoil. The entire lower surface experiences suction at this condition. A nearly constant, negative, pressure coefficient is observed on the aft portion of the lower surface. This high suction region extends from  $1.0 < x/c < 0.7$ , for the baseline airfoil and  $1.0 < x/c < 0.85$  for the reflex cambered airfoil. Downstream of this low pressure region, a gradual increase in pressure is observed towards the nose of the airfoil for the baseline airfoil, while the reflex cambered airfoil experiences a more sudden pressure recovery.

On the upper surface of the airfoils, shown in red, the pressure coefficient is equal to one (flow stagnation) at the trailing-edge, and falls to negative values, indicating suction, near the midsection of the airfoil. The upper and lower surface pressures are both negative at  $x/c \leq 0.2$ , with  $C_p = -0.5$ . Towards the nose of the airfoil, the pressure recovers slightly to a value of  $C_p = -0.33$  for the baseline airfoil and  $C_p = -0.2$  for the reflex cambered airfoil.

The pressure acting on the airfoil surface produces a force normal to that surface, either inward in the case of positive pressure or outward in the case of suction. The pressure drag (here referred to simply as drag) is the sum of the component of surface forces acting in the direction of the free-stream. Pressure forces acting on a surface with a normal perpendicular to the free stream will not contribute to pressure drag (although they will strongly affect lift), while forces acting on surfaces with a normal in the direction of the free stream, such as at the nose of the airfoil, will contribute strongly to drag. Figure 8 shows the pressure distribution from the wind tunnel measurements around the airfoils resolved in the direction of the oncoming flow. The extent of the colored area in the stream-wise direction corresponds to the magnitude of the pressure coefficient. Visualized in this manner, the colored area is proportional to the force acting on the airfoil in the stream-wise direction. The regions in orange correspond to pressure forces acting in the direction of the flow (positive drag) while the regions in blue represent forces acting to reduce drag. These figures are useful in understanding the primary contributors to reverse flow drag of the baseline airfoil and the main sources for improvement for the reflex cambered airfoil.

Figure 8 shows the drag visualization at  $\alpha = 184^\circ$ , and  $\alpha = 190^\circ$  for both the baseline and reflex cambered airfoil. For the baseline airfoil, over all angles of attack, the positive pressure on the upper surface over the aft section of the airfoil is a contributor to the drag, as well as the suction over the rounded nose. The positive pressure on the upper surface represents ram pressure as the incoming flow impacts this surface. This positive pressure region grows larger as angle of attack increases and the area normal to the flow direction increases as indicated by the larger orange region on the upper surface at  $\alpha = 190^\circ$ .

At  $\alpha = 184^\circ$ , downstream of  $x/c = 0.7$ , the baseline airfoil experiences suction on both the upper and lower surfaces of

the airfoil. Upstream of the thickest region of the airfoil, this suction acts to reduce drag, as seen by the blue regions while further downstream, the suction contributes to drag, shown as the orange regions around the nose of the airfoil. At  $\alpha = 190^\circ$ , the surface area perpendicular to the flow has increased, causing the pressure forces to act over larger areas. This ultimately serves to increase drag, compared to the  $\alpha = 184^\circ$  case.

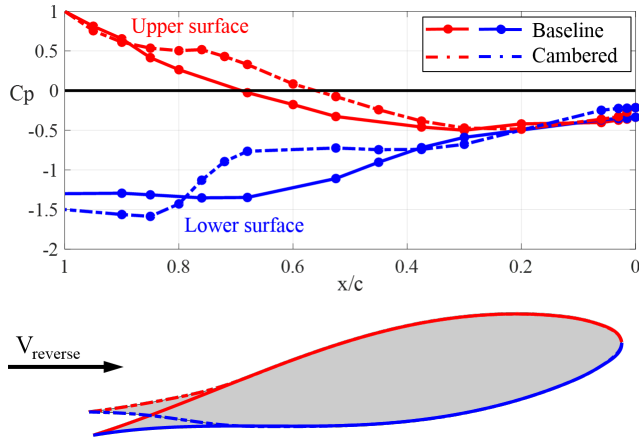


Fig. 7: Experimentally obtained pressure distributions for NACA 63-218 with and without  $10^\circ$  deflection of the trailing-edge section at  $\alpha=190^\circ$ . Red lines denote the upper surface and blue lines denote the lower surface.

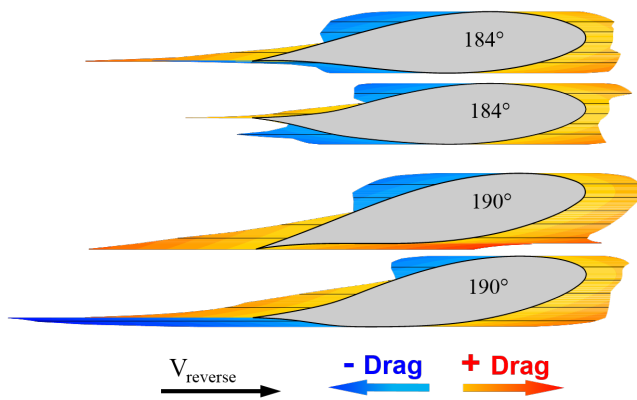
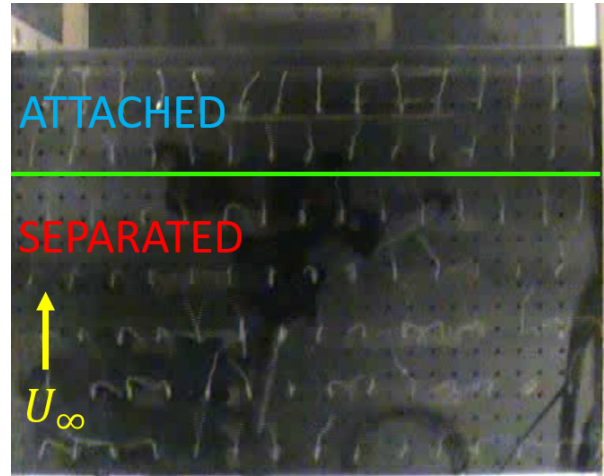


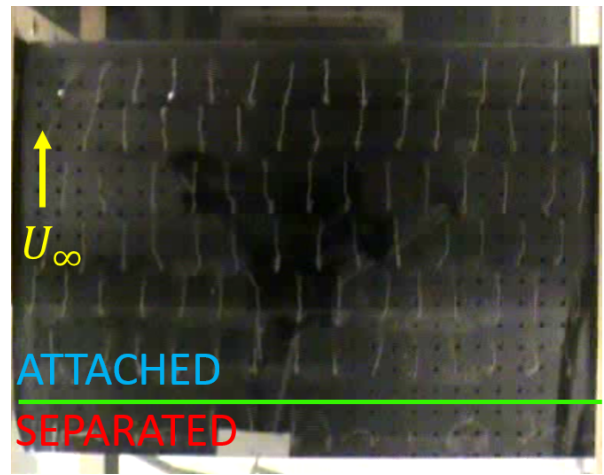
Fig. 8: Pressure drag on the NACA 63-218 with and without reflex camber at  $\alpha = 184^\circ$  and  $\alpha = 190^\circ$

For the reflex cambered airfoil, the area exposed to ram pressure on the upper surface (contributing to drag) is decreased compared to the baseline airfoil due to the change in orientation. Additionally, the aft section of the lower surface, which experiences a suction contributing to drag for the baseline airfoil is reoriented on the reflex cambered airfoil so that, while it still experiences suction, the suction now acts opposite the direction of the flow, subtracting from the drag. Comparing the suction over the round nose of the airfoil, the reflex cambered

case has slightly lower values of suction than the baseline airfoil, indicating that the deflection of the trailing-edge affects the flow downstream, leading to reduced pressure drag on the nose of the airfoil. This visualization indicates that there are two dominant sources of pressure drag reduction from adding reflex camber: a redistribution of the geometry near the geometric trailing-edge, and a global effect which increases pressure recovery near the geometric leading edge (round nose).



(a)



(b)

Fig. 9: Tuft flow visualization on the suction side of NACA 63-218 at  $\alpha = 190^\circ$ , for the baseline case (a), showing separation region and attachment line in green, and case with  $10^\circ$  trailing-edge reflex camber (b), showing earlier reattachment.

Flow visualizations using tufts can be used to show regions of separated and attached flow. Figure 9 shows the distribution of tufts placed on the lower surface of the airfoil at an angle of attack  $\alpha=190^\circ$  for the baseline case (Figure 9a) and reflex cambered case (Figure 9b). For the baseline case shown in Figure 9a, there is a clear region of separated flow where the tufts can be seen lifted off of the surface of the airfoil. Near the green line, unsteady reattachment is observed, where the tufts are attached to the surface of the airfoil but oscillate in

the spanwise direction. For the reflex cambered case shown in Figure 9b, the tufts are attached to the surface of the airfoil over nearly the entire length of the airfoil. The observed regions of separated flow show a qualitative comparison to the low pressure regions on the underside of the airfoil shown in Figure 7, suggesting the presence of separation bubbles that will experience large amounts of suction, with the suction decreasing as the flow reattaches.

### CFD Simulations of NACA 63-218 with and without 10° Reflex Camber

CFD simulations were carried out for the same airfoil geometry and at the same conditions as the wind tunnel experiment. 2D unsteady N-S and URANS/SA simulations were run for angles of attack from  $180^\circ < \alpha < 194^\circ$  in  $2^\circ$  increments. 3D DES simulations were also run for the baseline airfoil at  $182^\circ$ ,  $186^\circ$ , and  $190^\circ$ . The 2D N-S simulations without the turbulence model are laminar in regions of attached flow, so they are referred to as laminar, although large scale turbulence and unsteadiness was observed for these simulations in the detached regions of the flow. The 2D RANS simulations incorporating the SA turbulence model are referred to as turbulent and the 3D DES simulations are referred to as DES. The DES simulations were only slightly unsteady while the turbulent simulations showed almost no unsteadiness. Hodora et. al. also observed turbulent URANS simulations to result in a steady wake due to the dissipative nature of the turbulence model in Ref. 16.

All of the simulations were run for until the mean values of lift, drag, and moment stabilized, which was within about 20-40 chord passages. Only the forces due to pressure are shown here so that they may be compared with the data from the experiment, which was obtained by pressure integration.

Figure 10 shows a comparison of the lift, drag, and moment coefficients from the CFD simulations and the experiment. The values shown are time averages of the unsteady data over the last five chord passages. Both the laminar and turbulent simulations under predict the lift curve slope, causing the lift coefficient to be under-predicted at moderate angles of attack (around  $\alpha = 190^\circ$ ) for both the baseline and reflex cambered airfoil. The laminar simulations show a larger peak lift coefficient compared to both the experiment and the turbulent simulations. The DES simulations show very similar trends as the two dimensional turbulent simulations although the lift is slightly lower at  $\alpha = 186^\circ$ . The laminar simulations had a highly unsteady flowfield, represented by the vertical bars in the figure, which indicate one standard deviation of the lift, drag, or moment coefficient. The pitching moment shows similar trends as the lift as it is largely driven by the lift acting at the 3/4 chord location.

The laminar simulations over-predict the experimentally measured drag at low angles of attack, but correlate better with experiment at angles of attack above  $190^\circ$ . The turbulent simulations, especially for the baseline airfoil, correlate well with the experimental drag at low angles of attack ( $180^\circ - 188^\circ$ ),

but begin to under-predict it as the angle of attack increases beyond  $\alpha = 190^\circ$ . While laminar simulations generally over-predict the drag and turbulent/DES simulations generally under-predict drag, vis-a-vis the experimental results, the CFD simulations do predict the reduction in drag with introduction of reflex camber that was observed in the experiment.

Figure 11 summarizes the reduction in the drag (difference between baseline and reflex cambered airfoil drag) as a function of aerodynamic angle of attack. The largest reduction in drag from the wind-tunnel experiments was determined to be 50% relative to the baseline airfoil, at an aerodynamic angle of  $188^\circ$ . Also shown on Figure 11 are drag reductions from the CFD simulations. The turbulent simulations show a larger percentage reduction, around 60% at moderate angles of attack while the drag reduction in the laminar simulations is 20%-40%. It is noteworthy that both the wind-tunnel tests as well as CFD simulations show significant drag reduction over a fairly broad range of airfoil pitch variation.

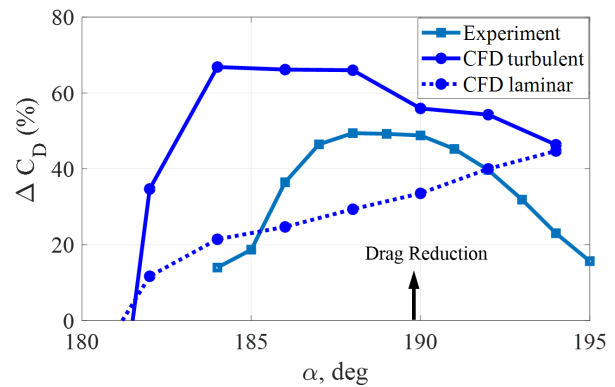


Fig. 11: Difference in drag between baseline NACA 63-218 and variation with 10° reflex camber.

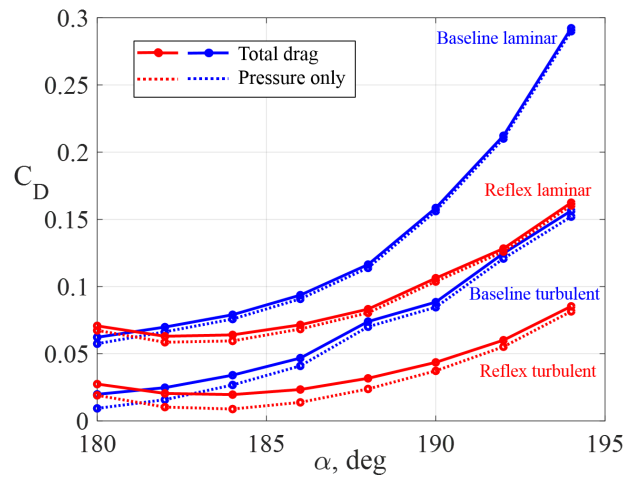


Fig. 12: Pressure drag and total (pressure + viscous) drag for CFD simulations of baseline NACA 63-218 and variation with 10° reflex camber.

The shear stress on the airfoil also contributes to the total drag

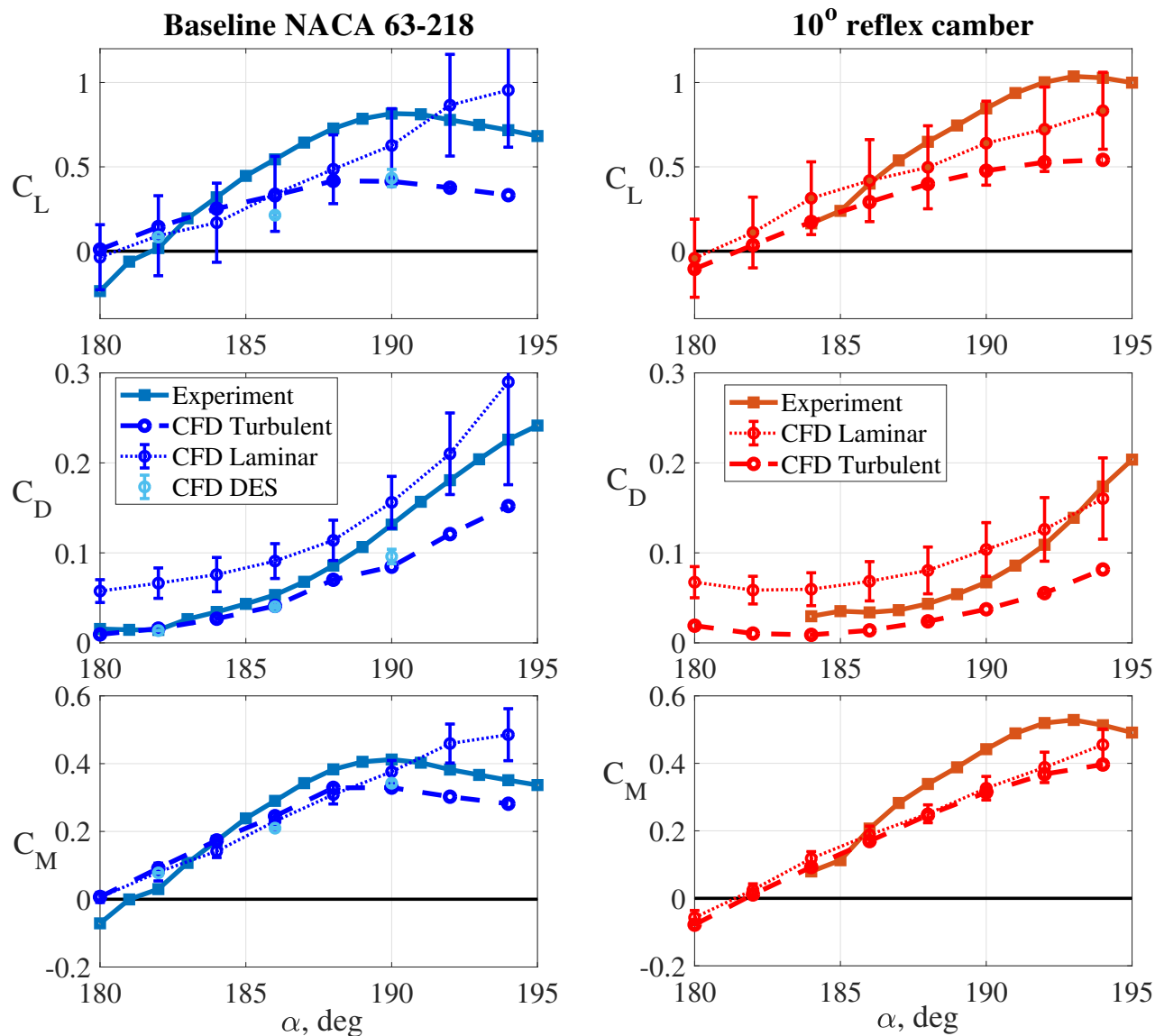


Fig. 10: Lift, drag, and moment (pressure component only) from experiments and CFD simulations for baseline NACA 63-218 (left) and variation with  $10^\circ$  deflection of trailing-edge section (right).

and is known as viscous or skin friction drag. Figure 12 shows the pressure drag for the CFD simulations along with the total drag, including the viscous component. The figure shows that at low angles of attack the viscous drag accounts for roughly half of the total drag. At higher angles of attack, the pressure drag grows rapidly while the viscous drag stays roughly the same, becoming only a small fraction of the total.

**CFD simulations at  $\alpha = 184^\circ$**  Figure 13 shows the flow-field around the airfoil at  $184^\circ$  angle of attack ( $4^\circ$  nose up in reverse flow) for the laminar and turbulent simulations. The flow shown is a time average of the unsteady flow over multiple chord passages. For the baseline airfoil, the flow is mostly attached, with the exception of a small separation bubble on the lower surface, and bluff body separation on the rounded nose of the airfoil downstream. These regions of the flow are captured both in the laminar and turbulent simulations. The

most notable differences between the two simulations is the size of the separation bubble near the trailing-edge and the extent of the separation region at the nose of the airfoil, the laminar simulation shows a smaller separation bubble, and a larger bluff body separation region, while the turbulent flow remains attached over a greater portion of the nose. These observations are in line with the broad understanding that flow with a turbulent boundary layer is better able to stay attached over bluff bodies than flow with a laminar boundary layer (Ref. 18).

The flowfields for the  $10^\circ$  reflex cambered airfoil are also shown in Figure 13. For both simulations, the separation bubble near the trailing-edge of the airfoil is eliminated with the introduction of the reflex camber and the flow is attached over most of the length of the airfoil. Similar to the baseline airfoil, the laminar simulation predicts a flow that separates from the rounded nose earlier than the turbulent simulation.

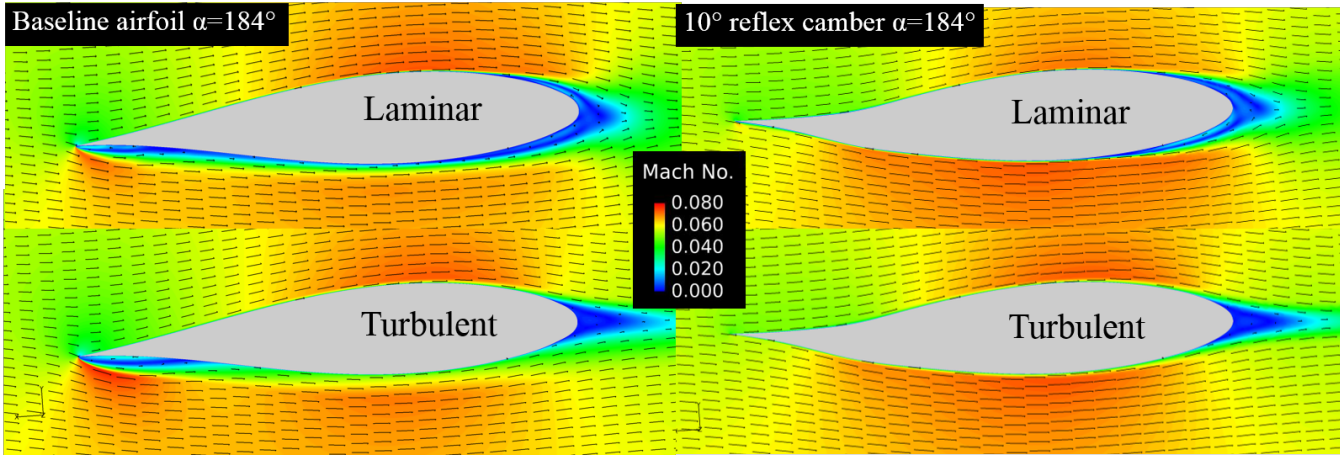


Fig. 13: Flowfields for the baseline NACA 63-218 and the reflex cambered airfoil at  $\alpha = 184^\circ$

In all of the simulations, the flow is generally fastest around the thickest sections of the airfoil, indicated by the dark red regions. There is also a region of faster moving air just outside of the separation bubble in the baseline cases.

The corresponding surface pressure for the two simulations and the experiment at  $184^\circ$  angle of attack are shown in Figure 14. For the baseline airfoil, near  $x/c = 1$  (the sharp geometric trailing-edge), the pressure approaches  $C_p = 1$  on the upper surface indicating stagnation and a region of ram pressure. There is also a strong suction region on the lower surface, with a suction of about  $C_p = -0.8$  near the trailing-edge. The low pressure regions near the trailing-edge for the laminar and turbulent simulations are coincident with the separation bubbles seen in Figure 13, with the separation bubble and corresponding low pressure region in the laminar simulation being slightly smaller than that in the turbulent simulation. The experimental pressure distribution shows a similar trend, although the low pressure region marking the separation bubble is slightly larger than both of the CFD simulations.

Both of the CFD solutions slightly under predict the suction on both surfaces of the baseline airfoil in the midsection ( $x/c$  of 0.4 - 0.8) where the flow is accelerated and the pressure reduced. As the flow approaches the nose of the airfoil, the pressure rises. The laminar flow simulation shows less pressure recovery, under-predicting that occurring during the experiment, while the turbulent simulation over-predicts the pressure recovery. This difference in pressure recovery is the primary source of difference in drag predictions at low angles of attack, with greater suction at the nose of the airfoil in the laminar simulation leading to higher overall drag.

In the simulations for the reflex cambered airfoil, the suction region near the trailing-edge on the lower surface is no longer observed, indicating that the oncoming flow stays attached over the lower surface. Near  $x/c = .75$ , the effect of the increased curvature can be seen as the pressure slightly increases on the upper surface and decreases on the lower surface. Downstream of the deflected section the pressure is qualitatively similar to the baseline airfoil. The laminar simulations again predict more suction around the nose of the

foil than the experiment while the turbulent simulation predicted a large pressure recovery and positive pressure around the nose of the airfoil.

These same surface pressures are shown in the streamwise direction for the experiment and the two simulations on the baseline airfoil in Figure 15. The rounded nose of the airfoil has a large area perpendicular to the flow, and so the pressure acting there will strongly influence the overall drag. Differences in the pressure over the nose of the airfoil in the experiment as well as the simulations are seen to drastically alter the total drag produced. The laminar simulation predicts the lowest pressure at the nose of the airfoil, and as a result, a large amount of drag force in this region and a greater integrated drag. The turbulent simulation predicts the highest pressure on the nose of the airfoil, resulting in a large reduction in the drag produced by the nose of the airfoil and the lowest integrated drag.

Figure 16 shows the pressure acting in the stream-wise direction for the reflex cambered airfoil at  $184^\circ$ . Much like the baseline airfoil, the drag is highly sensitive to the pressure at the nose of the airfoil, and differences in this pressure between the laminar and turbulent predictions lead to significant differences in the overall drag predictions.

For both the baseline airfoil in Figure 15 and the reflex cambered airfoil in Figure 16, the drag produced near the trailing-edge is similar to the experiment, while the drag produced near the nose of the airfoil is largely responsible for the difference in drag predictions.

**CFD simulations at  $\alpha = 190^\circ$**  Figure 17 shows the time-averaged flowfields for the baseline and reflex cambered airfoils at  $\alpha = 190^\circ$ . For the baseline airfoil, the separation region near the trailing-edge of the airfoil, which was small at  $\alpha = 184^\circ$ , has now grown significantly. Recirculation can also be seen, resulting in a non zero velocity near the surface. The laminar simulation shows a thicker and stronger recirculation region while the fully turbulent simulation shows a thinner, but longer recirculation region. Also included is the time av-

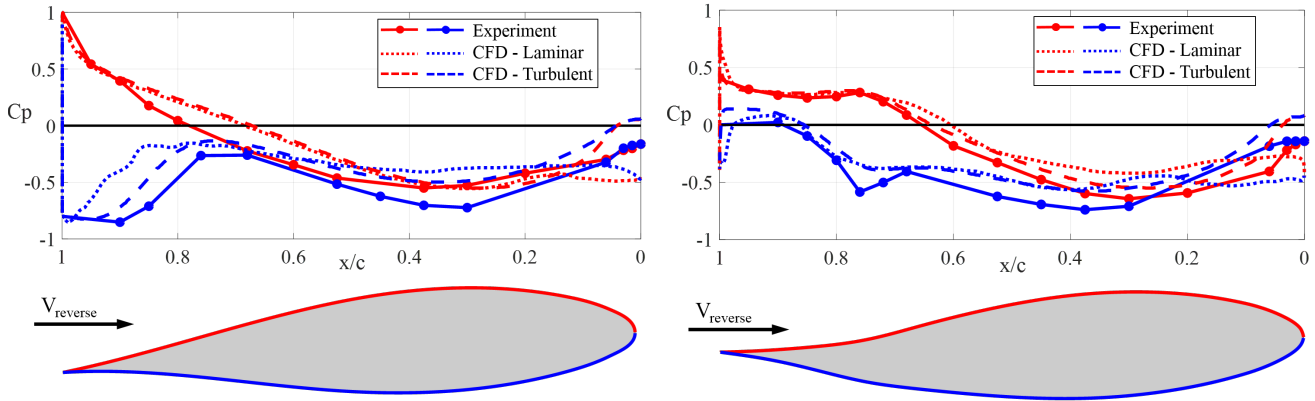


Fig. 14: Pressure distributions for baseline NACA 63-218 (left) and 10° reflex cambered airfoil (right) at  $\alpha=184^\circ$ . Red lines denote upper surface, blue lines denote lower surface.

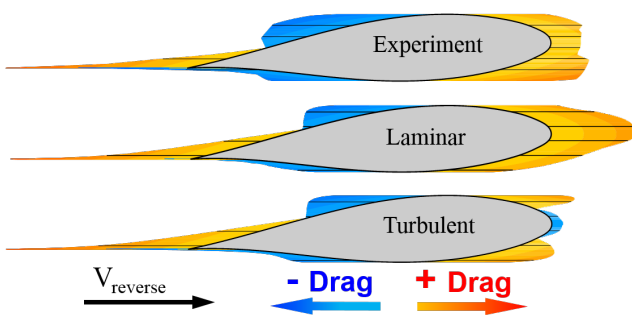


Fig. 15: Pressure drag contributions for the Baseline NACA 63-128 at  $\alpha = 184^\circ$  in the experiment (top) compared with laminar CFD (middle) and turbulent CFD (bottom) simulations

eraged flowfield for the DES simulation, which shows a separation region similar in size to the turbulent simulation, but with a slightly different velocity distribution. Downstream of the recirculation region, the flow reattaches before the maximum thickness of the airfoil. On the upper surface of the airfoil the flow remains attached until it reaches the nose. As with the  $\alpha = 184^\circ$  case, the laminar simulation shows earlier separation than the turbulent.

With the introduction of reflex camber, the size of the separation bubble on the lower surface is greatly reduced compared to the baseline airfoil and flow remains attached over most of the lower surface in both laminar and turbulent simulations. Comparing the upper surface to the lower, the boundary layer on the lower surface is much thicker than for the upper. This may be attributed to the separation bubble causing transition from laminar to turbulent flow and affecting the boundary layer downstream. When separated, a laminar flow can quickly transition to turbulent and reattach (Ref. 19). In all cases, bluff body separation is observed as the flow leaves the airfoil around the blunt nose, the separated region being larger for the laminar flow simulation.

Figure 18 shows the surface pressure for the experiments and

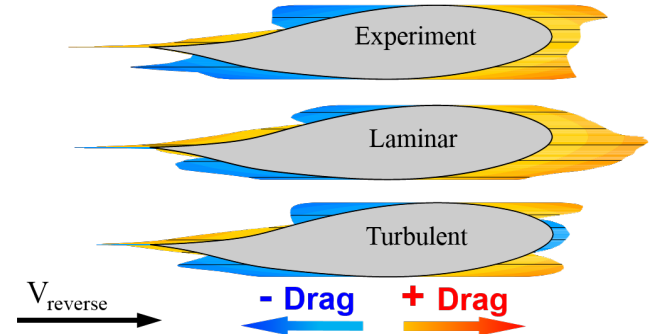


Fig. 16: Pressure drag contributions for the NACA 63-128 with 10° reflex camber at  $\alpha = 184^\circ$  in the experiment (top) compared with laminar CFD (middle) and turbulent CFD (bottom) simulations

CFD simulations at  $\alpha=190^\circ$ . As with the  $\alpha = 184^\circ$  case, the pressure reaches  $C_p = 1$  on the upper surface near the trailing-edge for both the baseline and reflex cambered cases. For the baseline airfoil there is a significant suction region on the lower surface, beginning at the trailing-edge. As with the  $\alpha = 184^\circ$  case, the rise in pressure is roughly coincident with the reattachment point seen in the flow visualizations. The laminar simulation predicts similar magnitudes of suction as the experiment, around  $C_p = -1.3$ , while the turbulent simulation slightly under-predicts the suction. The pressure for the DES simulation is very close to the turbulent simulation.

Overall, the experiment shows greater suction over most of the lower surface than either simulation for the baseline airfoil. The experiment shows the pressure recovering to  $C_p = -.33$  at the nose of the airfoil. As with the  $184^\circ$  case, the laminar simulation shows less pressure recovery than the experiment ( $C_p = -.42$  at the nose), leading to slightly higher drag while the turbulent simulation shows greater recovery ( $C_p = -.09$ ), leading to lower drag.

The surface pressure for the reflex cambered airfoil at  $\alpha = 190^\circ$  shown in Figure 18 shows a very close correlation for the pressure on the upper surface between the experiment and

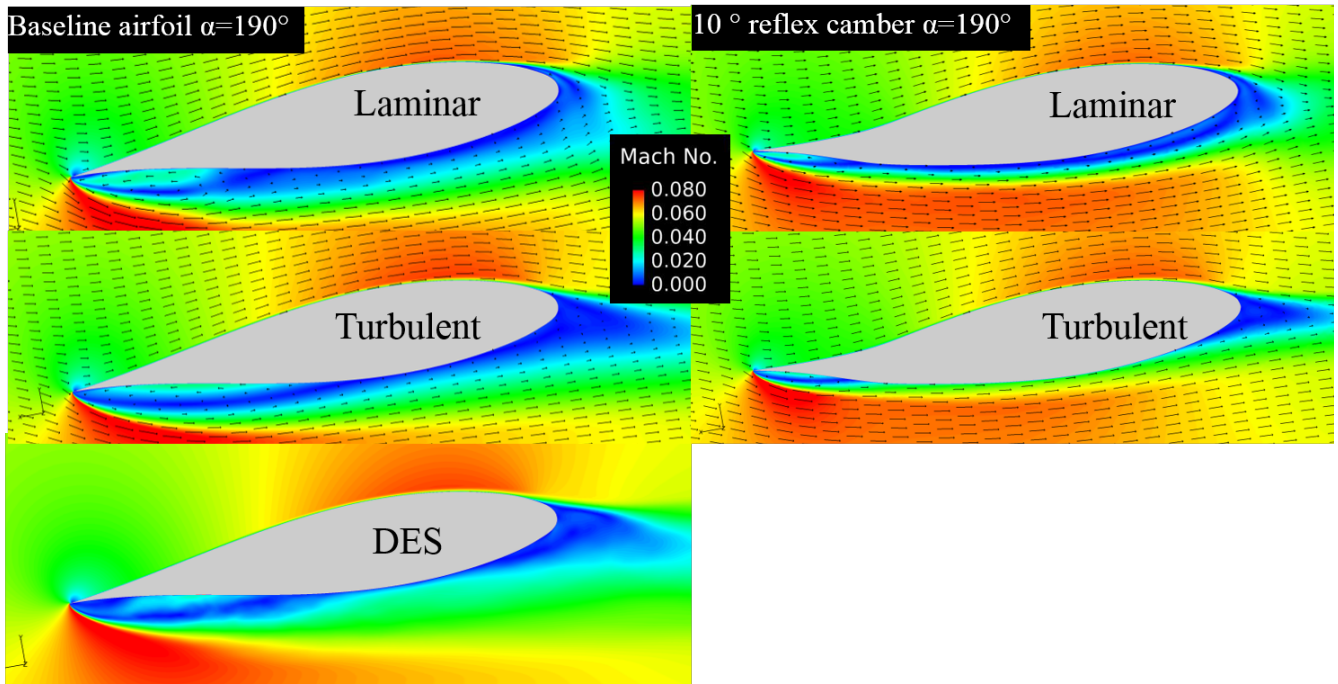


Fig. 17: Flowfields for the NACA 63-218 and the same airfoil with 10° reflex camber at  $\alpha = 190^\circ$

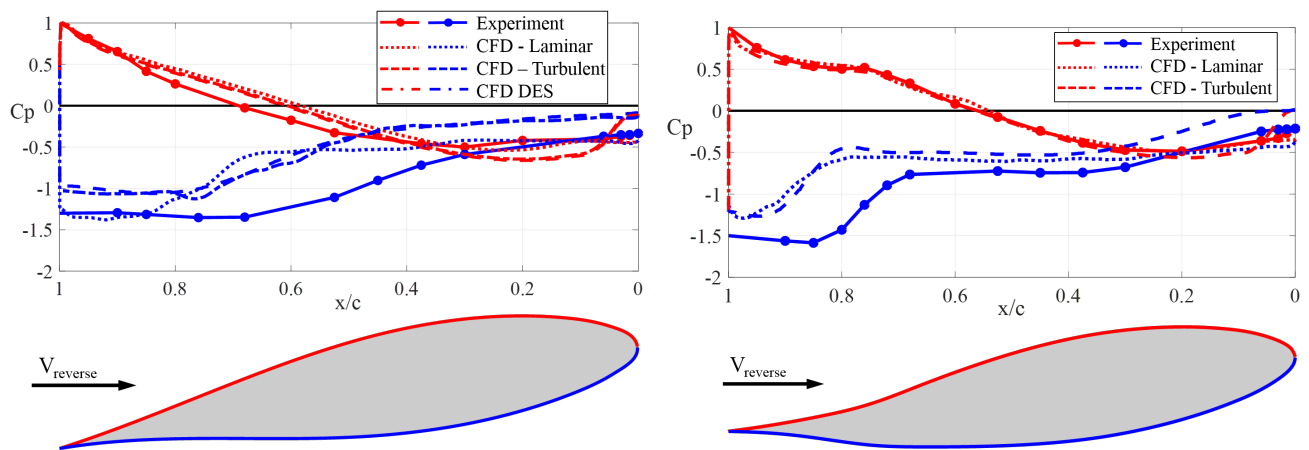


Fig. 18: Pressure distributions for baseline NACA 63-218 and the same airfoil with 10° reflex camber at  $\alpha = 190^\circ$ . Red lines denote upper surface, blue lines denote lower surface.

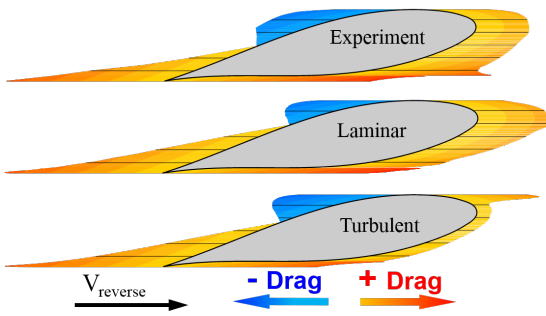


Fig. 19: Pressure drag contributions for the baseline NACA 63-218 at  $\alpha = 190^\circ$  in the experiment (top) compared with laminar CFD (middle) and turbulent CFD (bottom) simulations

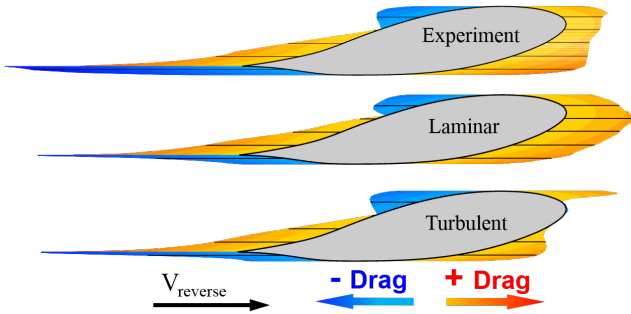


Fig. 20: Pressure drag contributions for the NACA 63-218 with  $10^\circ$  reflex camber at  $190^\circ$  in the experiment (top) compared with laminar CFD (middle) and turbulent CFD (bottom) simulations

both of the CFD simulations. Both of the CFD simulations under predict the magnitude of the peak suction on the lower surface as well as the extent of the separation bubble. As with all of the other cases, the laminar simulation under-predicts the pressure at the nose and the turbulent simulation over-predicts it.

Figure 19 Shows the pressure drag contributions for the baseline experiment and two simulations at  $\alpha = 190^\circ$ . As with the  $\alpha = 184^\circ$  case, the simulations show similar drag contributions to the experiment near the trailing-edge and differences in drag contributions near the nose. While the experiment showed significantly more suction than the simulations over the the lower surface of the airfoil between  $0.4 < x/c < 0.8$ , this has a small impact on drag as this surface is nearly tangential to the flow. Closer to the nose, the difference in pressure predictions is seen to have a much greater impact on drag, with the laminar simulation predicting a slightly higher amount of suction drag than the experiment and the turbulent simulation under-predicting it.

Figure 20 shows the drag contributions at  $\alpha = 190^\circ$  for the reflex cambered airfoil. Again, both simulations show qualitatively similar results as the experiment near the trailing-edge. The drag reduction due to rotation of the trailing-edge section seen in the experiment is well captured in both CFD simulations. Reiterating the observations seen in the experiment,

the most striking differences between the baseline airfoil and reflex cambered airfoil are the reduction in the size of the positive pressure (drag contributing) region near the trailing-edge on the upper surface, and the direction in which the suction near the trailing-edge on the lower surface acts. Both of these effects are seen in all three cases (experiment and two types of simulation) and serve to reduce the overall drag on the airfoil. The suction (or lack thereof) over the nose of the airfoil is seen to be responsible for most of the discrepancy between the CFD simulations and the experiment.

### CFD Simulations of NACA 63-218 with $15^\circ$ reflex Camber

In addition to the airfoil with a  $10^\circ$  of deflection of the trailing-edge section, 2D RANS/SA simulations were conducted on the same NACA 63-218 with a  $15^\circ$  deflection of the trailing-edge section.

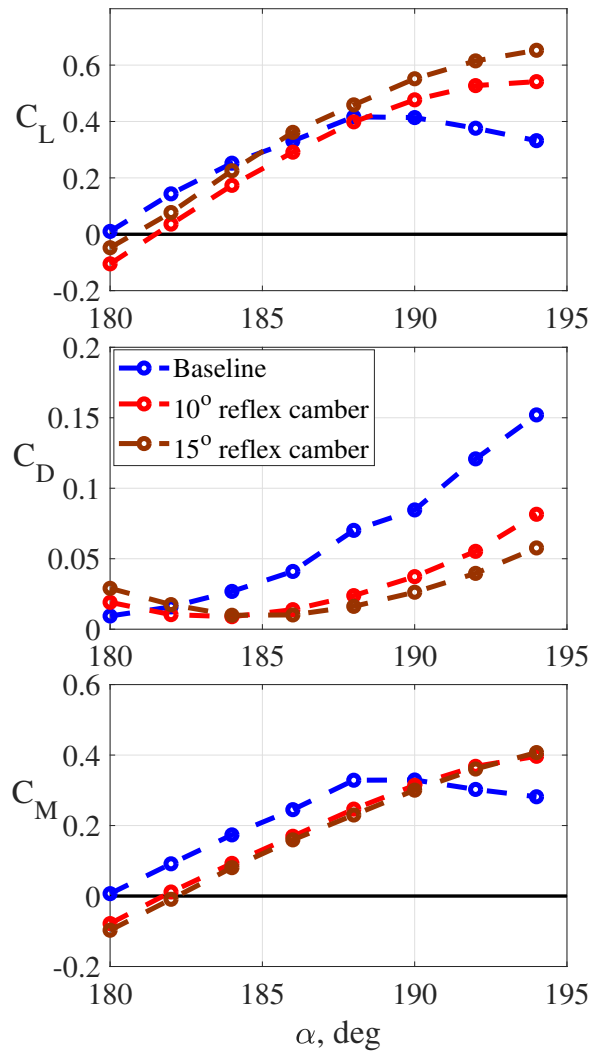


Fig. 21: Lift, drag, and, pitching moment for airfoils with  $0^\circ$  (baseline),  $10^\circ$ , and  $15^\circ$  reflex camber using turbulent RANS/SA simulations

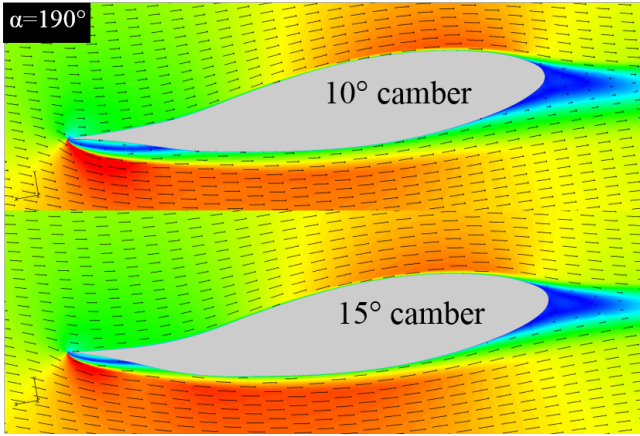


Fig. 22: Flowfields for airfoils with 10° and 15° reflex camber at  $\alpha = 190^\circ$  from turbulent RANS/SA simulation

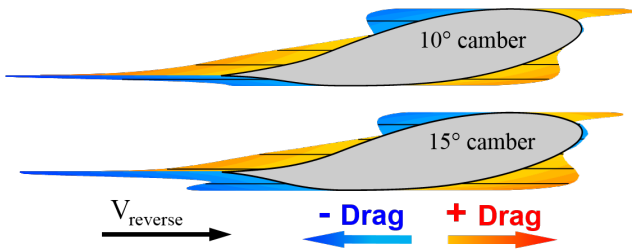


Fig. 23: Pressure drag on airfoils with 10° and 15° reflex camber from turbulent RANS/SA simulations

Figure 21 shows a comparison of the lift, drag, and moment of the 15° reflex cambered airfoil compared to the 10° reflex cambered variant as well as the baseline. The 15° reflex cambered case is shown to slightly increase lift coefficient at all angles of attack, as well as further decrease drag at angles of attack above 185°. The drag increases with the amount of camber at low angles of attack (close to  $\alpha = 180^\circ$ ) indicating that at these low angles, introducing reflex camber would only be detrimental and that the reflex camber is only effective at reducing drag at moderate to high pitch angles in reverse flow. It can be reasoned that at each angle of attack, there is a specific deflection of the trailing-edge that will lead to the minimum drag. The pitching moment is decreased only slightly for the 15° camber airfoil as compared to the 10° case.

Figure 22 shows the flowfields for the airfoils with 10° and 15° reflex camber of the trailing-edge section at  $\alpha = 190^\circ$ . The 15° cambered airfoil shows a smaller separation bubble, as well as a thinner boundary layer on the lower surface.

Figure 23 shows the pressure drag contributions for the 10° and 15° reflex cambered airfoils. The larger deflection of the trailing-edge further reduces the exposure of the upper surface to ram drag, and also increases the area on the lower surface exposed to forward-pulling suction.

**High-speed simulations** 2D Turbulent RANS/SA simulations were also run with a higher speed,  $Re = 1.5$  million, and larger chord,  $c = 0.475m$ , representative of airfoils in operation on a high-speed helicopter, such as the XH-59A. Figure

24 shows the lift, drag, and moment coefficients for the baseline and 15° reflex cambered airfoil at these conditions. For both the baseline and 15° cambered airfoils, there is negligible difference in the lift, drag, and moment compared to the low speed condition. The reduction in drag due to reflex camber, however, is still significant at moderate angles of attack.

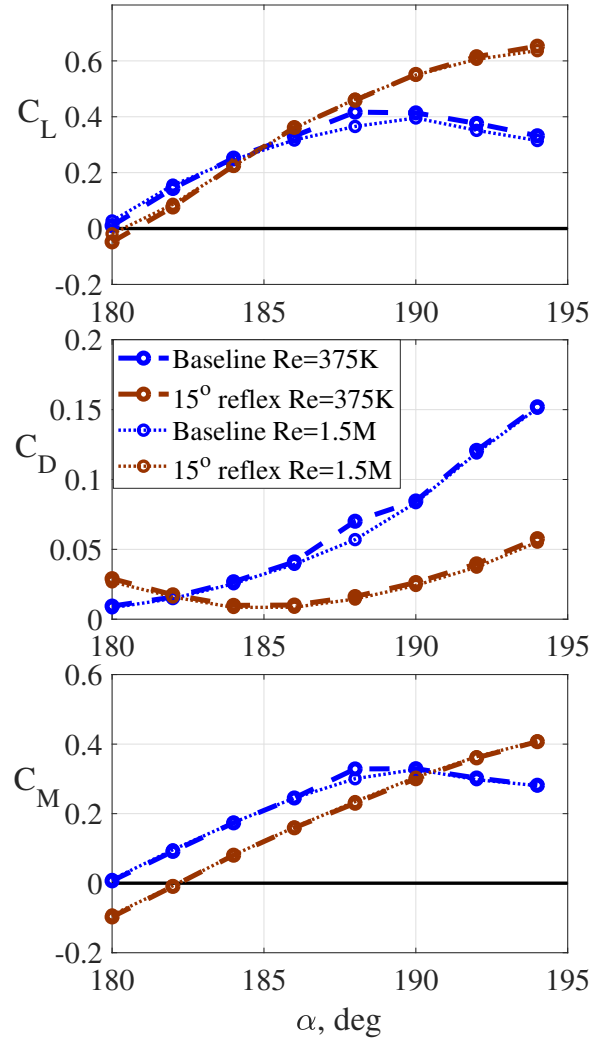


Fig. 24: Comparison of airfoils with 0° and 15° reflex camber at  $Re = 375,000$  and  $Re = 1.5$  million, from turbulent RANS/SA simulations

Figure 25 summarizes the reduction in drag for the airfoil with 15° reflex camber. At both low and high Reynolds numbers the drag reduction computed with turbulent RANS is predicted to be greater than 70% at moderate angles of attack, with little difference in the percentage reduction between the  $Re = 375,000$  and  $Re = 1.5$  million speed cases.

## CONCLUSION

Through experiment and the use of computational fluid dynamics, this study examines a NACA 63-218 airfoil in reverse

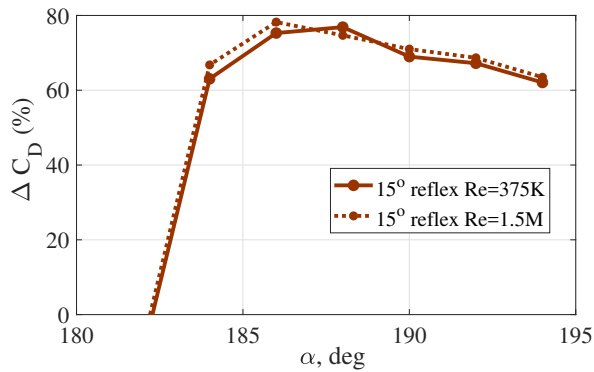


Fig. 25: Drag reduction with addition of 15° reflex camber at  $Re = 375,000$  and  $Re = 1.5$  million

flow conditions at  $Re = 375,000$ , specifically focusing on the use of reflex camber to improve the aerodynamic operating state (and reduce drag) at positive pitch attitudes up to 15° in reverse flow. From the results in this study, the following observations were drawn:

1. In reverse flow conditions, the baseline airfoil displays a separation bubble on the lower surface at the geometric trailing-edge. At low to moderate airfoil pitch angles, the flow reattaches further downstream. A region of constant pressure (suction) is observed corresponding to the separation bubble, followed by a region of pressure recovery corresponding to reattachment. On the upper surface close to the geometric trailing-edge, the airfoil experiences significant ram pressure. This transitions to a region of suction over the mid-chord section as the flow accelerates over the upper surface. At the rounded nose of the airfoil, significant bluff body separation can be observed.
2. For a positive pitch attitude, the introduction of reflex camber, better aligns the geometric trailing-edge to the oncoming flow. At low pitch angles, the separation bubble at the trailing-edge is completely eliminated. At moderate pitch angles, the bubble length reduces relative to the baseline airfoil, and pressure recovery occurs earlier. Part of the drag reduction with reflex camber is attributed to reduced exposure to ram drag on the upper surface due to change in trailing-edge geometry. Due to this same change in geometry, the suction in the vicinity of the trailing-edge of the lower surface rotates to now oppose to the direction of flow, thereby contributing to further reduction in drag.
3. The wind tunnel experiment showed drag reductions of up to 50% with a trailing-edge reflex angle of 10°, relative to the baseline. The overall drag of the airfoil in reverse flow from CFD simulations showed significant differences from the experiment, but this is primarily due to poor prediction of bluff body separation at the airfoil nose. However, the CFD simulations are able to capture the drag reduction with reflex camber (predicted to be up

to 60% from the 2D URANS simulations with SA turbulence model) as this is governed by the changes in the trailing-edge region, independent of bluff body separation at the nose.

4. CFD simulations were also conducted at a higher reflex angle of 15°. A 15° reflex camber was seen to produce larger drag reduction than 10° reflex camber for any airfoil pitch attitude greater than 5°. At 10° pitch attitude, 15° reflex produced a drag reduction in excess of 70% (compared to 60% with a 10° reflex).
5. CFD simulations were also conducted at a Reynolds number of 1.5 million, representative of conditions occurring on a large coaxial rotor or slowed rotor compound helicopters during high-speed flight. At these conditions, the overall drag for both the baseline airfoil and the airfoil with 15° reflex camber were predicted to be very similar to that at  $Re = 375,000$  and the reduction in drag due to the reflex camber was predicted to be in excess of 70%.

## REFERENCES

- <sup>1</sup>Bagai, A., “Aerodynamic Design of the X2 Technology Demonstrator™ Main Rotor Blade,” 64th Annual Forum of the American Helicopter Society, Montreal, Canada, April 2008.
- <sup>2</sup>Giovanetti, E. B. and Hall, K. C., “A Variational Approach to Multipoint Aerodynamic Optimization of Conventional and Coaxial Helicopter Rotors,” AHS 71st Annual Forum, 2015.
- <sup>3</sup>Hersey, S., Sridharan, A., and Celi, R., “Multiobjective Performance Optimization of a Coaxial Compound Rotorcraft Configuration,” Fifth Decennial AHS Aeromechanics Specialists Conference, San Francisco, CA, Jan 2014.
- <sup>4</sup>Naumann, A., “Pressure Distribution on Wings in Reversed Flow,” Technical Report 1011, National Advisory Committee for Aeronautics, 1942.
- <sup>5</sup>Critzos, C. C., Heyson, H. H., and Jr., R. W. B., “Aerodynamic Characteristics of NACA 0012 Airfoil Section at Angles of Attack From 0 to 180,” Technical Note 3361, National Advisory Committee for Aeronautics, 1955.
- <sup>6</sup>Pope, A. Y., “The Forces and Pressures Over an NACA 0015 Airfoil Through 180 Degrees Angle of Attack,” 1947.
- <sup>7</sup>Leishman, J. G., “Aerodynamic Characteristics of a Helicopter rotor Airfoil as Affected by Simulated Ballistic Damage,” Technical report, Army Research Laboratory, 1993.
- <sup>8</sup>Lind, A. H., Lefebvre, J. N., and Jones, A. R., “Experimental Investigation of Reverse Flow Over Sharp and Blunt Trailing Edge Airfoils,” 31st AIAA Applied Aerodynamics Conference, 2013.

<sup>9</sup>Lind, A. H., Lefebvre, J. N., and Jones, A. R., “Time-Averaged Aerodynamics of Sharp and Blunt Trailing-Edge Static Airfoils in Reverse Flow,” *AIAA Journal*, Vol. 52, (12), December 2014, pp. 2751–2764.  
doi: DOI: 10.2514/1.J052967

<sup>10</sup>Lind, A. H. and Jones, A. R., “Vortex Shedding from Airfoils in Reverse Flow,” *AIAA Journal*, Vol. 53, (9), 2015, pp. 2621–2633.  
doi: DOI: 10.2514/1.J053764

<sup>11</sup>Lind, A. H., Smith, L. R., Milluzzo, J. I., and Jones, A. R., “Reynolds Number Effects on Rotor Blade Sections in Reverse Flow,” *Journal of Aircraft*, Vol. 53, (5), 2016.

<sup>12</sup>Lind, A. H. and Jones, A. R., “Unsteady Airloads on Static Airfoils Through High Angles of Attack and in Reverse Flow,” *Journal of Fluids and Structures*, Vol. 63, 2016, pp. 259–279.

<sup>13</sup>Smith, L. R., Lind, A. H., Jacobson, K. E., Smith, M. J., and Jones, A. R., “Experimental and Computational Investigation of a Linearly Pitching NACA 0012 in Reverse Flow,” AHS 72nd Annual Forum, West Palm Beach, 2016.

<sup>14</sup>Smith, M. J., Liggett, N. D., and Koukol, B. C., “Aerodynamics of Airfoils at High and Reverse Angles of Attack,” *Journal of Aircraft*, Vol. 48, (6), 2011, pp. 2012–2023.  
doi: DOI: 10.2514/1.C031428

<sup>15</sup>Hodara, J. and Smith, M. J., “Improvement of Crossflow Aerodynamic Predictions for forward Flight at All Advance Ratios,” 40th European Rotorcraft Forum, 2014.

<sup>16</sup>Hodara, J., Lind, A. H., Jones, A. R., and Smith, M. J., “Collaborative Investigation of the Aerodynamic Behavior of Airfoils in Reverse Flow,” AHS 71st Annual Forum, May 2015.

<sup>17</sup>Andrew M. Wissink, a. B. J. and Sitaraman, J., “An Assessment of the Dual Mesh Paradigm Using Different Near-Body Solvers in Helios,” 55th AIAA Aerospace Sciences Meeting, 2017.  
doi: 10.2514/6.2017-0287

<sup>18</sup>Panton, R. L., *Incompressible Flow*, John Wiley & Sons, Inc., third edition, 2005, Chapter 14, pp. 326–330.

<sup>19</sup>Bertin, J. J. and Cummings, R. M., *Aerodynamics for Engineers*, Pearson, fifth edition, 2009, Chapter 6, p. 298.